Soft Matter

Extracting Microscopic Insight from Transient Dielectric Measurements During Large Amplitude Oscillatory Shear

Journal:	*Soft Matter*
Manuscript ID	SM-ART-06-2023-000786.R2
Article Type:	Paper
Date Submitted by the Author:	23-Aug-2023
Complete List of Authors:	Cho, Noah; Northwestern University, Chemistry Shi, Jiachun; University of Illinois at Urbana-Champaign Murphy, Ryan; National Institute of Standards and Technology, NCNR Riley, John; Dow Chemical Co Collegeville Rogers, Simon; University of Illinois at Urbana-Champaign, Chemical and Biomolecular Engineering Richards, Jeffrey; Northwestern University, Chemical & Biological Engineering; Northwestern University

Soft Matter

ARTICLE TYPE

Cite this: DOI: 00.0000/xxxxxxxxxx

Extracting Microscopic Insight from Transient Dielectric Measurements During Large Amplitude Oscillatory Shear†

Noah H. Cho[a] Jiachun Shi,[b] Ryan P, Murphy[c] John K. Riley[d] Simon A. Rogers,[b] and Jeffrey J. Richards[a]

Received Date
Accepted Date

DOI: 00.0000/xxxxxxxxxx

Probing the transient microstructure of soft matter far from equilibrium is an ongoing challenge to understanding material processing. In this work, we investigate inverse worm-like micelles undergoing large amplitude oscillatory shear using time-resolved dielectric spectroscopy. By controlling the Weissenburg number, we compare the non-linear microstructure response of branched and unbranched worm-like micelles and isolate distinct elastic effects that manifest near flow reversal. We validate our dielectric measurements with small angle neutron scattering and employ sequence of physical processes to disentangle the elastic and viscous contributions of the stress.

1 Introduction

Developing techniques to study microscopic dynamics under steady and transient rheometric flows is critical to refine constitutive relationships that predict how materials respond to processing. For this purpose, in-situ rheometric techniques have proliferated where a rheometer is coupled to other measurement devices to gain access to structural or dynamical information during flow. These in-situ techniques include structural probes such as small angle scattering measurements[1–5] and particle tracking microscopy[6–9], dynamical probes such as superposition rheometry[9,10], nuclear magnetic resonance[11,12], and Raman spectroscopy[13,14], and techniques that afford both structure and dynamics such as X-ray photon correlation spectroscopy[15,16]. These in-situ rheometric methods are all motivated by understanding how the imposition of shear forces influences the dynamic or structural response of that system.

For decades, the rheo-dielectric technique[17? ,18], which combines dielectric and rheological measurements, has been used to study the dynamics of soft materials under flow. Initially motivated by the ability of dielectric spectroscopy to probe the reorientation of dipoles on small molecules and polymers[19], rheo-dielectric measurements have proliferated to a wide variety of material systems, where the combination of small amplitude oscillatory shear (SAOS) measurements with impedance spectroscopy can provide insight into thermal transitions, kinetic processes, and broadband dynamics.[20] Watanabe demonstrated how the use of the rheo-dielectric techniques to probe segmental dynamics of polymer chains in polymer solutions and melts could interrogate global motion chain motion as well as local segmental motion.[18] Further applications of the technique include microscale phase separation of block copolymers and reorientation of liquid crystal domains. Colby extended the linear viscoelastic rheology and dielectric approach to polyelectrolyte solutions,[22–24] where the dielectric response is dominated by a fluctuation of ions of the polyelectrolyte, so the ionic cloud around the chain. More recently, rheo-dielectric measurements have examined electrical charge transport in conjugated polymer organogels[25], dipolar reorientation in cross-linked elastomeric networks[26], concentrated inverse wormlike micelle solutions[27], and the electrical transport in suspensions of conductive nanomaterials[28–30].

The rheo-dielectric method has also been extended to materials far from equilibrium, including large amplitude oscillatory (LAOS) shear flows.[31,32] In these measurements, the transient stress and dielectric response functions are often qualitatively similar. However, because they have fundamentally different physical origins, unique insight can be gleaned from the evolution of the dielectric properties in shear flow.[33] For example, the

[a] Department of Chemical Biological Engineering, Northwestern University, Evanston, IL, USA. Tel: 847 467 4641; E-mail: jeffrey.richards@northwestern.edu
[b] Department of Chemical and Biomolecular Engineering, University of Illinois of Urbana-Champaign, Urbana, Illinois
[c] NIST Center for Neutron Research, National Institute of Standards and Technology, Gaithersburg, MD, USA
[d] Performance Materials Coatings, The Dow Chemical Company, Collegeville, Pennsylvania, USA

† Electronic Supplementary Information (ESI) available: [details of any supplementary information available should be included here]. See DOI: 10.1039/cXsm00000x/

‡ Additional footnotes to the title and authors can be included *e.g.* 'Present address:' or 'These authors contributed equally to this work' as above using the symbols: ‡, §, and ¶. Please place the appropriate symbol next to the author's name and include a `\footnotetext` entry in the the correct place in the list.

acceleration of global chain motion was observed under steady flows in solutions of linear and star poly(isoprene) chains. The frequency dependence of the dielectric response obtained during steady shearing was critical to evaluating the microscopic origin of this phenomenon. This work was extended to large amplitude oscillatory shear (LAOS), where the current adsorption method probed the dielectric response during transient flow.[32] The results of rheo-dielectric LAOS showed a transient decay and time-oscillatory electrical response that bore similarities to the steady shear response, but this technique was limited by the strong coupling between the LAOS field and the orientation distribution of the chain. Frequency-dependent dielectric measurements during LAOS have been attempted, but no effort was made to decouple the oscillatory nature of the deformation from the frequency-dependent dielectric response.

Obtaining the frequency-dependent dielectric response under transient flows such as LAOS presents considerable challenges because the time scale of the dielectric measurement is finite and often longer than the oscillation period. Therefore, it is challenging to decouple the transient microstructure response from the finite duration of the dielectric measurement. This was the case for Horio et. al[32] who observed an oscillatory current response of polyisoprene in polyisobutylene subjected to LAOS, whose period was inversely correlated with the LAOS oscillation frequency. To avoid this coupling, we perform rheo-dielectric measurements under the condition where the dielectric frequency, ω_ε, far exceeds the LAOS frequency, ω_{LAOS}, or $\omega_{LAOS} << \omega_\varepsilon$. In this way, the dielectric response probes the instantaneous microstructure of the sample at each time point within a LAOS cycle and the coupling to the LAOS field is negligible. Using this technique, we reconstruct the full frequency-dependent dielectric response of entangled, branched and unbranched inverse wormlike micelles (WLMs), lecithin micelles swollen with water in decane, as a function of Weissenberg number ($Wi = \tau_c \dot{\gamma}$ where τ_c is the characteristic relaxation time and $\dot{\gamma}$ is the shear rate) in LAOS flow. These worm-like micelles exhibit a complex dielectric response that for unbranched micelles consists of three primary relaxations, a high-frequency relaxation (2 MHz) arising due to rotation of the zwitterionic head groups[34] resulting in fluctuation of the local polarization, a middle frequency (kHz) relaxation associated with the rotation of unentangled micelles and the Rouse-like motion of micelle segments between entanglements[35], and a low-frequency relaxation that Cirkel et al attributed to global chain motion in dilute solution.[36]. The low frequency dielectric response originates from large-scale fluctuation of polarization of the micelles, which permit delocalization of charge from the micelle contour via intermicelle charge exchange. This charge exchange facilitates dc-conductivity and also causes electrode polarization at very low frequencies as ions accumulate at the electrode-liquid interface. The same intermicellar charge exchange results in a fluctuation of charge on each micelle which for fast processes such as Rouse and rotational motion of unentangle micelle segments is responsible for the middle frequency dielectric response as described in Cho et al.[35] When the water content is increased, a maximum in viscosity associated with the formation of branches that also significantly enhances the low frequency conductivity of the solutions. The enhancement of conductivity is similar to percolation behavior observed in water-in-oil microemeulsions where aggregates of droplets accelerate charge transport and the dielectric response is no longer fully correlated with the micellular dynamics but instead with the topology of the percolated emulsion network.

The frequency dependent dielectric response of branched and unbranched entangled WLMs have also been studied under steady flow.[27] In that work unbranched micelles showed a monotonic decrease of the dielectric response with increasing shear rate, which correlated with increasing anisotropy. The authors suggested that the flow of the unbranched micelles was dominated by the release of segments from constrained entanglements that once released could align in the flow. This is in contrast to the branched case, which showed a non-monotonic change in the low frequency dielectric response. They attributed this to the disruption of percolated network of branched micelles. They further showed that at high shear rates, dielectric response of both branched and unbranched micelles were nearly identical suggesting that once the branched micelles are broken the micelle segments will align regardless the topological state of the micelles.

While steady shear focuses on viscous effects only, the elastic response of the entangled micelle network should be particularly sensitive to branch breaking. As highlighted in steady shear, obtaining the broadband dielectric response of both branched and unbranched micelles is necessary to fully characterize important structural transitions that occur in steady flow. In this work, we seek to extend that framework to LAOS, where elastic effects can be observed during the flow reversal test. To do this, we subject branched and unbranched samples to the condition of steady alternance. For every cycle, we measure the complex impedance at a fixed frequency and then between cycles increment the frequency logarithmically to obtain the complete frequency dependence of the WLMs throughout the cycle. As this technique relies on the time-reproducibility of the transient microstructure at steady alternance, we verify this reproducibility using small angle neutron scattering (SANS) during LAOS. Using the combination of these three techniques, we show that it is possible to compare the transient dielectric response of branched and unbranched WLMs during LAOS. We find that for most of the cycle, the behavior of both the branched and unbranched samples was identical to that found in steady shear. However, we observe important dynamical differences that arise upon flow reversal where elastic effects dominate. We illustrate, that these differences would not have been distinguishable without obtaining the full frequency dependent response during transient LAOS. To further distinguish between the primarily elastic response and the viscous response of the WLMs, we employ sequence of physical processes (SPP)[37] that allows for the determination of the instantaneous viscous and loss modulus throughout the LOAS cycle. We use the transient moduli derived from SPP to identify dielectric features unique to elastic effects that appear in LAOS that are not present in the steady shear data.

2 Materials and Methods

2.1 Materials

Soy lecithin (purity, 95%) was used from Avanti Polar Lipids (Alabasterm, AL). The average molecular weight is 775.05 g/-mol. Chloroform (purity, 99.99%) and n-decane were purchased from Fisher Chemical (Chicago, IL). 18 MΩ deionized water (LabChem, Zelienople, PA) was used

2.2 Wormlike Micelle Preparation

The procedure for preparing branched and unbranched WLMs was adopted from the previous reference published by our group.[35] A concentrated stock solution of dried and purified lecithin lipid in decane was prepared at 50 mg/ml, and water-to-lipid molar ratio, $W = [H_2O]/[Lec] = 1.0$. Water was added to this stock solution to yield the desired water-to-lipid molar ratio. The transition from branched to unbranched micelles was confirmed by measuring viscosity in Figure S2, and the unbranched sample was chosen at W = 2.4, and the branched sample was chosen at 3.0 because they exhibited similar viscoelastic relaxation times (τ_c = 3.9 s ($W = 2.4$) and 3.8s ($W = 3.0$) in Figure S2 and Table S1.[27]

2.3 Rheo-dielectric Measurements

In-situ rheo-dielectric measurements were performed in the same manner in the prior reference.[27] Rheological measurements were made using a strain-controlled rheometer (ARES G2, TA instruments, New Castle, DE) equipped with a customized stainless-steel Couette geometry.[38] To prevent evaporation of n-decane and uptake of water from the gap of geometry, we used a solvent trap covered with Fomblin oil (Sigma-Aldrich LVAC 06/6, average molecular weight 1800). Also, a Teflon vacuum grease was applied to seal the physical gap between the cup and the top of the solvent trap. A Teflon tape was also wrapped around the edge of the solvent trap lid to minimize evaporation. We confirmed negligible water evaporation by repeating a SAOS measurement over a day and observed no change in the rheological behavior. For dielectric measurements, the same stainless-steel Couette geometry used for rheological measurements was applied to measure the complex impedance of WLMs over a frequency range of 20 Hz to 50 MHz with an impedance analyzer (E4990A, Keysight Technologies, Santa Rosa, CA). The potential amplitude was 100 mV. The measured impedance was then corrected for stray inductance and capacitance of the open cell and corrected using the known cell constant. The cell constant was determined by measuring conductivity with various potassium chloride solutions.

2.4 Rheo-SANS measurements

Small angle neutron scattering measurements were performed on the NG-3 45m very small angle neutron scattering (VSANS) instruments at the NIST Center for Neutron Research (NCNR) at the National Institute of Standards and Technology (NIST) in Gaithersburg, MD.[39] VSANS results were collected at a single configuration with nine guides, front detector distance of 1 m, and middle detector distance of 4.5 m to cover a Q-range from approximately 0.008 $Å^{-1}$ to 0.6 Å−1, where $Q = 4\pi/\lambda \sin(\theta/2)$, where λ is the neutron wavelength (6 Å, 0.12 FWHM) and θ is the total scattering angle. Subtracting for transmission, background, empty cell scattering measurements, and detector efficiency, the intensity profile as a function of the Q was reduced to absolute scale using the standard NCNR reduction macros in Igor Pro.[40] For rheo-SANS measurements, we used an MCR rheometer (Anton Parr, Graz, Austria) equipped with a titanium cup (30 mm inner diameter) and bob (29 mm outer diameter). Using custom-built Python protocols, event mode scattering data from the middle top, and bottom detectors of the VSANS instrument were combined to obtain high-quality scattering data for 51-time bins throughout the cycle. Counts within each time bin were summed from at least ten cycles during steady alternance to ensure that there were over 100 k counts on each slice.

2.5 Sequence of physical processes (SPP)

We use the sequence of physical processes[41] method to analyze the transient responses of the unbranched and branched WLMs to LAOS. The SPP analysis determines instantaneous elastic and viscous moduli, G'_t and G''_t that are partial derivatives of the stress with respect to strain and rate. The analysis was performed using open-source MATLAB-based software. Several studies have shown that SPP provides a sensitive set of transient measures linked to structural measures in a range of materials.[42–44] Beyond simply providing instantaneous elastic and viscous properties, the SPP analysis can be used to calculate the amount of recoverable strain of the system when $G'_t >> G''_t$.

3 Rheo-dielectric Response to Steady Shear

Prior to performing LAOS, we prepared a series of 50 mg/mL samples of lecithin in decane swollen with water that form entangled worm-like micelle solutions chains with a known molar water-to-surfactant ratio, $W = [H_2O]/[Lec]$ = 2.0 - 3.4. We performed small amplitude oscillatory shear (SAOS) experiments on each sample at 25 ^{o}C, and confirmed they were entangled by the observation of an elastic plateau modulus, G_p, at high frequencies and a low-frequency terminal scaling $G'' \sim \omega$ and $G' \sim \omega^2$, where G' is storage modulus, G'' is loss modulus and ω is frequency. We then calculate the dynamic viscosity, $\eta_0 = \lim_{\omega \to 0} G''/\omega$, at each water content.

These samples are known to undergo a topological transition from unbranched to branched micelles as the water content increases. We determined this transition by a maximum in the viscosity at W = 2.7. Beyond this maximum, we observe a continued increase in the plateau modulus and the conductivity measured using dielectric spectroscopy indicating the formation and proliferation of branched micelles. These results are summarized in Figure S1-S3 and Table S1. Based on these measurements, we selected two samples consisting of unbranched micelles with $W = 2.4$ and branched micelles with $W = 3.0$ for further testing. These samples were chosen because they have similar characteristic relaxation times, $\tau_c = \frac{1}{\omega_c} = 3.2s$ (unbranched) and 3.8s (branched), where ω_c was determined from the cross-over frequency of the storage G' and loss modulus G'' showing the low-

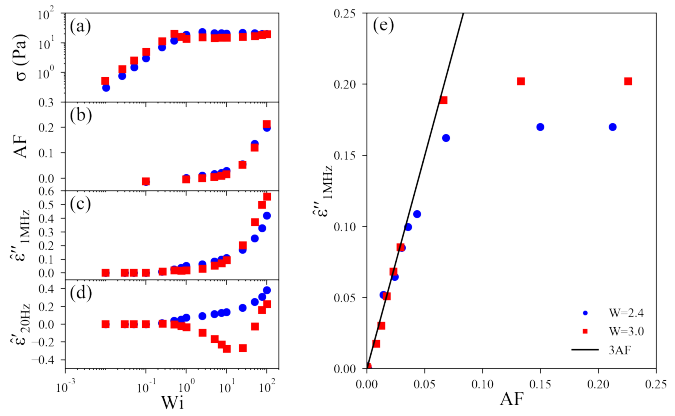

Fig. 1 Steady-state dielectric rheology with SANS results between unbranched (blue) and branched (red) WLMs as a function of Wi. A.) steady state stress, b.) anisotropy factor at segmental length scale, Q = 0.04 Å^{-1}, c.) normalized dielectric loss at high frequency, 1 MHz d.) normalized dielectric constant at low frequency, 20 Hz. E.) normalized dielectric loss at high frequency as a function of alignment factor with a solid black line representing $\hat{\varepsilon}'' = 3AF$.

frequency terminal regime.

Following the protocol developed by Riley et al.[27], we performed dielectric rheology and rheo-SANS measurements on these samples under steady shear, which consisted of acquiring structural and dielectric spectra of each sample as a function of the Wi. At each Wi, we performed small angle neutron scattering experiments (SANS) where we accumulated a 2-D scattering pattern as a function of the scattering wavevector, Q. These measurements use multiple detectors to acquire scattering data over a larger Q-range as compared to traditional SANS measurements. We performed an annular average of the detector array at Q=0.04 Å^{-1} after correcting the raw scattering data for an empty cell and converting it to an absolute scale. Riley et al. showed that this Q-range is appropriate to capture the segmental alignment of the micelle chains in simple shear flow as this length scale corresponds to distances larger than the micelle cross-section and smaller than the micelle persistence length. Thus the AF probes the orientation of micelle segments projected onto the 1-3 plane of shear. Using these azimuthal averages, we calculated the anisotropy factor, AF, using Eq. (1).[45]

$$AF = \frac{\int_0^{2\pi} I(Q^*,\phi)\cos(2\phi)d\phi}{\int_0^{2\pi} I(Q^*\phi)d\phi} \quad (1)$$

The steady-state stress and the AF for both W = 2.4 and W = 3.0 samples are summarized in Figure 1(a) and 1(b). The two samples exhibit very similar stress and AF trends as a function of Wi. In fact, both samples show the transition to strong anisotropy at a Wi = 10, consistent with other studies that have found the stress plateau is associated with shear banding.[46,47] The 2-D SANS patterns for each Wi are given in Figure S5.

We also performed rheo-dielectric measurements on both samples. The frequency-dependent impedance was measured at each shear rate and corrected for the stray inductance and resistance of the geometry to complex dielectric response ($\varepsilon^* = \varepsilon' - i\varepsilon''$) where ε' is dielectric constant and ε'' is dielectric loss). The dielectric spectra showed a complex frequency dependence that, in prior work, has been shown to contain information about the Rouse and rotational dynamics of the micelle chains.[34–36] We observed the dielectric loss ε'' at high frequency (1 MHz) decreased monotonically with increasing shear intensity, which was strongly correlated with the increase in AF for both branched and unbranched samples. Motivated by this, we have chosen to normalize the shear-dependent dielectric properties using $\hat{\varepsilon}'' = 1 - \frac{\varepsilon''(\dot{\gamma})}{\varepsilon''(\dot{\gamma}=0)}$ as shown in Figure 1.(c). $\hat{\varepsilon}''$ does not change significantly when Wi is less than one because the system remains undisturbed by the shear flow. With increasing Wi, ε'' increases, and we observed that this increase was frequency-independent.48 In contrast, the normalized real component of the permittivity, $\hat{\varepsilon}' = 1 - \frac{\varepsilon'(\dot{\gamma})}{\varepsilon'(\dot{\gamma}=0)}$ is shown as a function of Wi for W = 2.4 and W = 3.0 samples. While the qualitative behavior of the high-frequency response for both samples is similar (not shown), the low-frequency behavior of the branched sample exhibits a non-monotonic change in the real component of the permittivity at intermediate Wi as shown in Figure 1(d). This results in a negative $\hat{\varepsilon}'$ which is notably absent in the unbranched samples. These results are identical to Riley et al., where the non-monotonic change in ε' was attributed to the enhanced mobility of branched segments as the network was broken under flow.[27]

4 Rheo-dielectric Response to Large Amplitude Oscillatory Shear (LAOS)

To obtain the transient dielectric response during transient flow, we subject the unbranched sample (W = 2.4) to LAOS at De = 0.1 and Wi = 25, where the Deborah number (De) is the dimensionless frequency given as $\omega\tau_c$. Note that the ratio of the Wi to the De gives the strain amplitude of the oscillation. The strain waveform is shown in Figure 2(a). After one half cycle, the sample achieved steady alternance, as indicated by the reproducibility of the stress waveform (Figure 2(b)), and we commenced our dielectric measurements. We perform LAOS at a fixed De and Wi while recording the transient impedance of the sample during each cycle. At the end of each LAOS cycle, we increase the dielectric frequency such that over the course 51 LAOS cycles, the frequency changes from 20 Hz to 10 MHz on a logarithmic scale. The frequencies applied for the first nine cycle are shown in Figure 2(c). In this way, we obtain the frequency dependent impedance of the sample at every time point within a cycle.

A comparison of transient stress and $\hat{\varepsilon}''$ for one cycle is plotted in Figure 2(d-f) versus the period, T. The sample's dielectric properties were sensitive to this LAOS condition and were symmetric about the axis of zero strain. We also observe significant elastic effects during LAOS, which result in the appearance of stress overshoots after flow reversal. To emphasize this, we examine the sample's response at strategic positions throughout the cycle, as indicated by the colored markers in Figure 2(d-f). These markers span the region of the strain wave where the shear rate passes through zero and where the elastic response of the WLM network is evident. At the blue point, which corresponds to the zero-shear rate and stress condition, we see a minimum in the $\hat{\varepsilon}''$, which cor-

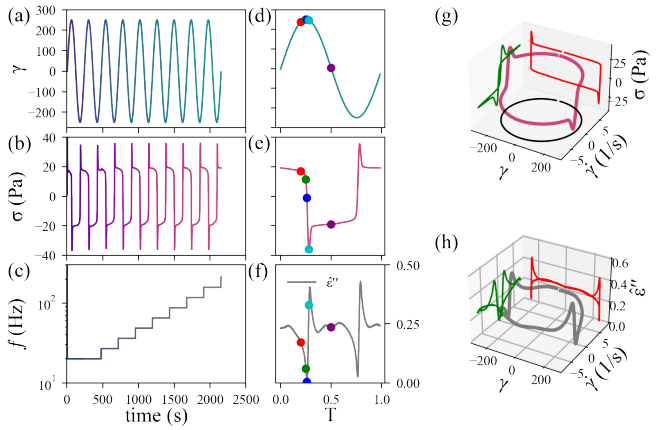

Fig. 2 Summary of rheo-dielectric measurements using LAOS (C_{lec}= 50 mg/ml, $W = 2.4$, $Wi = 25$, $De = 0.1$). a.) applied strain b.) stress c.) frequency versus real-time measurements. d.) step strain e.) step stress f.) step normalized dielectric loss versus period determined by the cycle time. Each color point matches the points of strain, stress, and complex permittivity, respectively. g.) 3D projection plot of LAOS flow (brown) functions of strain, shear rate, and stress. 2D projection of elastic response (red) and viscous response (green) are plotted on both axes. h.) 3D projection plot of the normalized dielectric loss response as a function of strain and shear rate.

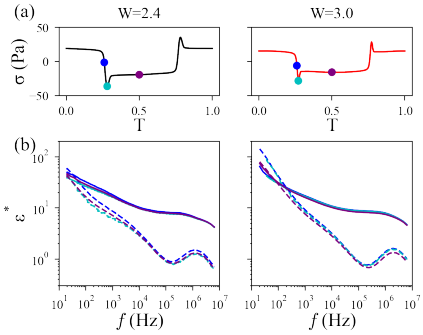

Fig. 3 Rheo-dielectric spectra at each stress bin at $Wi = 25$ and $De = 0.1$ for $W = 2.4$ (left) and $W = 3.0$ (right). a.) transient stress versus the period and b.) complex permittivity (solid line – real component, dashed line – imaginary component) vs. frequency (Hz). The colored markers match the color of the dielectric spectra.

responds to the state of minimum alignment. The sample then experiences the transient equivalent of a startup test where $\hat{\varepsilon}''$ passes through a maximum value before transitioning to steady shear. These signals are shown as viscous and elastic projections in Figure 2(g) and 2(h). Comparing their shapes highlight the rich non-linear phenomena associated with these LAOS deformation conditions.

The protocol described to produce Figure 2 allows for the further reorganization of the dielectric response of each sample during LAOS. Following the state points highlighted in Figure 3, we can bin the complex permittivity measured at each frequency in adjacent cycles to discrete time points sampled within the deformation period. Because the microstructure under steady alternance is time periodic[37], each point within a period represents a unique microstructural state, and the frequency-dependent permittivity is a probe of that structure at that state point. The complex permittivity can then be utilized with an appropriate model to obtain quantitative microscopic insight under transient conditions. However, in this work, our focus is the qualitative comparison of steady shear to LAOS for these two samples. As such, we compare $W = 2.4$ and W = 3.0 samples under the same LAOS conditions in Figure 3 ($Wi = 25$, $De = 0.1$). The associated transient shear stress is shown in Figure 3(a) for each sample, and the reorganized frequency-dependent complex permittivity is shown in Figure 3(b). Note that the minimum frequency of our dielectric measurements far exceeds the frequency applied in LAOS. The colors of the state points shown in Figure 3(a) correspond to the colors of the dielectric data associated with those points in the cycle.

The dielectric spectra shown in Figure 3(b) demonstrate that our method can distinguish between the evolution of the microstructure between the unbranched and branched samples throughout the LAOS cycle with excellent temporal resolution. Following the sequence of state points associated with the transient stress, we observe a startup (blue marker) that transitions to a stress overshoot (cyan marker), and then both samples achieve steady flow (purple marker) by the middle of the cycle. The observed transient stress signals are quantitatively like one another and show little evidence that the presence of branches influences the stress. However, when the dielectric spectra are examined, distinct differences emerge, particularly at low frequencies in the dielectric loss. The unbranched samples show a maximum in the dielectric loss at zero shear rate (blue), a minimum in the dielectric loss at the peak of the stress overshoot (cyan), and then an intermediate value upon transition to steady shear (purple). In contrast, the branched sample showed a minimum in the dielectric loss of low-frequency at the steady shear condition, while the zero-shear rate and stress overshoot condition are almost identical. These spectral differences demonstrate that the unbranched and branched samples exhibit important microstructural differences as they transition from startup to flow. The distinction between the dielectric behavior at low frequency between unbranched and branched WLMs is qualitatively similar to that observed in steady flow for this system.[27]

These differences are persistent for all Wi for these two samples. They can be visualized by calculating the frequency dependence of $\hat{\varepsilon}''$ at each Wi tested and mapping it at each point in the period and frequency, f. This is shown in Figure 44 for the branched and unbranched samples as a function of Wi (1, 10, 25, 50, and 100). All images have the same scale, and differences in the spectral features of the dielectric data are evident when comparing $W = 2.4$ (top) and $W = 3.0$ (bottom) at each Wi. A bright band appears at the cycle period, $T \sim 0.22$ and 0.74, corresponding to the maximum stress overshoot across all Wi in the $W = 2.4$ sample. This band is absent or significantly diminished in all the $W = 3.0$ samples. The magnitude of $\hat{\varepsilon}''$ at $T = 0.5$ is most dramatic at low frequencies and high Wi for the $W = 2.4$ and $W = 3.0$ samples. This is consistent with what is observed in steady shear, where the low-frequency dielectric data show an

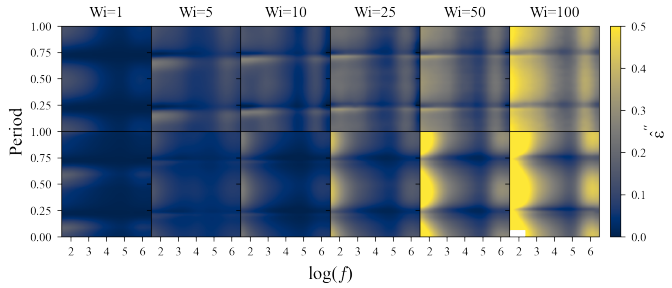

Fig. 4 Transient dielectric data collected as a function of Wi for samples $W = 2.4$ and $W = 3.0$. Each pixel within an image represents the average $\hat{\varepsilon}''$ with the x-axis corresponding to the log of the dielectric frequency, f, and y-axis representing the time within the cycle period, T. The color scale is set to vary linearly from 0 to 0.5 using the "cividis" colormap in Matplotlib.

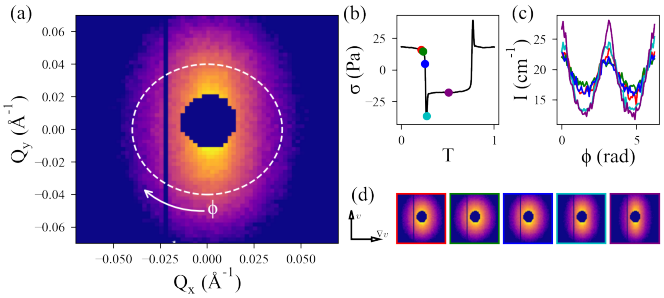

Fig. 5 Rheo-SANS profiles on unbranched WLMs ($W = 2.4$, $C_{lec} = 50$ mg/ml) at $Wi = 100$. a.) representative 2D SANS pattern in the 1-3 plane of shear, b.) stress response of LAOS measured during rheo-SANS, c.) Absolute scattering intensity on 1D annular average profiles was used to quantify anisotropy via alignment factor. d.) 2D SANS patterns of representative stress values. Each plot color is matched with the same color dots in Figure 2(b).

enhancement in the dielectric loss at intermediate Wi.

5 Microstructural Response to LAOS

To compare the rich features of the dielectric data in LAOS flow with those observed in steady shear, it is necessary to examine the evolution of the WLM microstructure in LAOS. Therefore, using the same conditions as in 4, we performed rheo-SANS experiments $W = 2.4$ and $W = 3.0$ samples. Note that these measurements were performed on different days and with different preparations, so the relaxation times of the samples were slightly different from those measured in the above section, $\tau_c = 5.0$ s (unbranched) and 5.6 s (branched). These experiments were performed on the VSANS instrument at NIST, and the measurements were conducted in the 1-3 (flow-vorticity) plane of shear. One challenge with utilizing the VSANS instrument for these experiments is that event mode data is accumulated on multiple detector carriages, each with its detector reference frame. Further, the acquisition was divided over multiple event mode files, so we combined event mode data files into discrete slices that could be averaged and reduced. Using this approach, we reconstructed the LAOS cycle for each sample at each condition. An example of a pair of detectors mapped to the sample reference frame and plotted in absolute scale is shown in Figure 5(a). The middle left and middle right detector carriages are shown, which combined left a small gap (the vertical line at $Q_x = 0.023$ Å $^{-1}$). This gap between the detectors, the beam stop area, and the detector edges were masked prior to subsequent analysis.

By examining slices strategically chosen at similar cycle times as in Figure 2(d), we can observe the evolution of the microstructure in LAOS flow for the condition of Wi = 100 in Figure 2(b-c). We observed a minimum alignment at the blue point, corresponding to the zero-shear rate condition. However, the alignment remains finite until a few strain units after reversal, indicating that the network has not fully relaxed upon reversal. Performing annular averages at Q=0.04 Å^{-1}, as shown in Figure 5(c) of the 2D slices associated with each point shown in the sequence of 2D images in Figure 5(d), we can observe the change in anisotropy throughout the cycle with the maximum in anisotropy at this Wi being associated with the maximum in the shear rate.

Repeating these rheo-SANS measurements at each Wi and for each water content, we were able to calculate the AF at all conditions. This along with the transient stress is shown in Figures 6. We observed that, as the Wi increases, the magnitude of the maximum anisotropy achieved within a cycle increases. It is also apparent that the magnitude of the AF at $T = 0.5$ are similar for the branched and unbranched samples and consistent with the observed AF in steady shear for both samples. This is expected as the De is small enough that the sample has sufficient time for the deformation throughout the cycle to mimic the structure in steady flow. However, significant differences between the unbranched and branched samples appear when examining the part of the cycle where elastic effects are dominant. The unbranched sample exhibits a local maximum in AF near the position in the cycle that corresponds to the stress overshoot. Meanwhile, the branched sample shows no local maximum in AF near the stress overshoot, and instead, the AF appears to be out of phase with the strain, suggesting that a viscous response dominates the AF. This indicates that the microscopic consequence of the startup and stress overshoot in the branched sample does not affect the magnitude of the AF, but in the unbranched sample, its influence is evident.

With the AF calculated at each Wi and for each sample, we can correlate changes in stress and AF to changes in $\hat{\varepsilon}'$, and $\hat{\varepsilon}'$ as shown in Figures 6 throughout the cycle between unbranched and branched WLMs. We focus on two dielectric frequencies, 48 Hz and 1.1 MHz, which correspond to the brightest regions in Figure 4. With increasing Wi, we observed an enhancement of the nonlinear stress response, evidenced by the increased prevalence of the stress overshoot. This stress overshoot occurred for both the branched and unbranched samples. This increased prevalence correlated well with an enhancement of the AF with increasing Wi for the unbranched sample. In the branched sample, we observed no strong correlation between the stress overshoot and the alignment factor. For the unbranched sample, these trends continued in the dielectric response at both 48 Hz and 1.1 MHz, where the maximum in $\hat{\varepsilon}'$ and $\hat{\varepsilon}''$ both correlated well with the position and magnitude of the stress overshoot. The branched sample's dielectric and AF responses were much more complicated. In

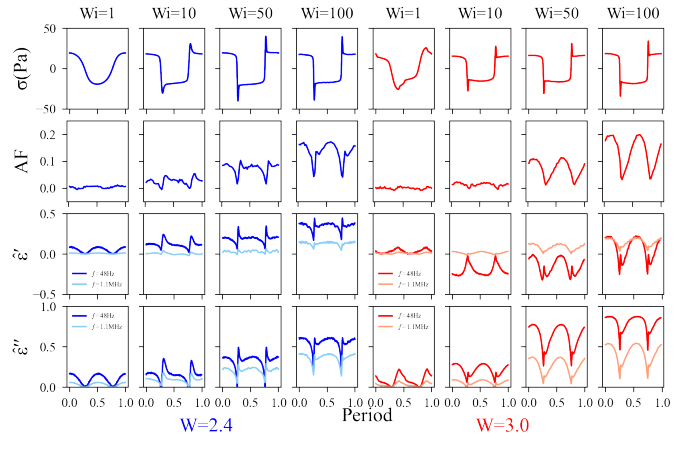

Fig. 6 Summary of rheological, dielectric, and SANS measurements as a function of Wi for unbranched (blue, left) and branched (red, right) WLMs at W = 2.4 and W = 3.0, respectively. The rows from top to bottom are the shear stress, the alignment factor, $\hat{\varepsilon}'$ and $\hat{\varepsilon}''$ for dielectric frequencies, 48 Hz and 1.1 MHz versus the oscillation period.

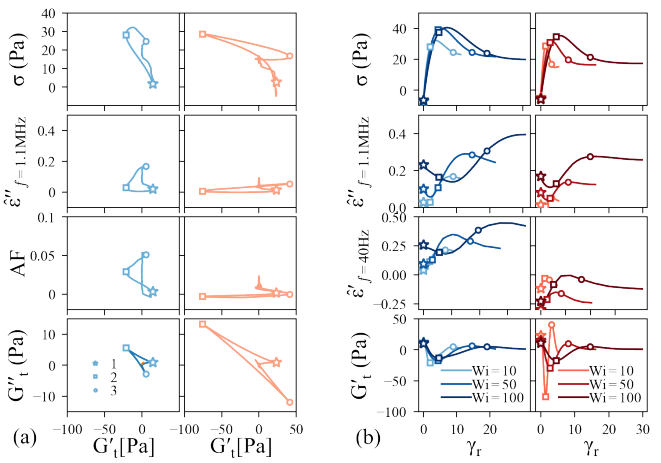

Fig. 7 (a) From top to bottom: shear stress, normalized dielectric loss at 1 MHz, alignment factor, and transient loss modulus versus the transient storage modulus for unbranched (blue, left) and branched (red, right) wormlike micelle solution at Wi=10. Star, square, and circle markers point out the apex values of each quadrant of the Nyquist representation. (b) shear stress, normalized dielectric loss at 1 MHz, normalized dielectric permittivity at 48 Hz, and transient storage modulus versus the strain since flow reversal. Symbols are the same as in (a) and the applied Wi is given in the legend.

particular, the peak in AF associated with the stress overshoot observed in the unbranched sample is absent in the branched sample above Wi = 10, and instead, the AF correlates well with the maximum in the shear rate. Similar qualitative behavior was evident in $\hat{\varepsilon}''$ at both frequencies, 48 Hz and 1.1 MHz, the dielectric response correlates well with the AF, but there is no apparent correlation with the stress overshoot for $Wi > 10$. The largest differences between the alignment factor and the dielectric response of both samples under LAOS emerge at low frequencies where the dielectric response originates from large-scale structural fluctuations that cannot relax during LAOS. At these very low frequencies, the degree of coupling to LAOS can become significant and impact the oscillatory dielectric response. This was the case in Horio et al.[32].

6 Sequence of Physical Processes (SPP)

The results above highlight the ability of our rheo-dielectric method to resolve transient dielectric features associated with non-linear deformation and to probe elastic effects during LAOS. To go beyond qualitative comparison, we utilize the sequence of physical processes (SPP) analysis to isolate the elastic response of the micelle network from the viscous response during the transient deformation. SPP analysis provides a model-independent method to interpret time-oscillatory deformations, including steady alternance during LAOS.[41] The results of SPP applied to our data are summarized in Figure 7 (a) for the unbranched and branched case. Shown in Figure 7 (a) is a one half-cycle ($\dot{\gamma} > 0$) for the Wi=10 case. For this half-cycle, we determined the transient dynamic moduli, G_t' and G_t'', and show σ, ε'', AF, and G_t'' versus G_t'. The star, square, and circle markers are included to guide the eye and are positioned at the apex of each quadrant of the Nyquist representation of the G_t'' versus G_t'.[48] When elastic effects are dominant, the dynamic moduli are non-zero and return to the origin of the Nyquist representation (G_t'' versus G_t') when viscous effects dominate, By comparing the apexes to the transient stress, the star marker corresponds closely with the start of the flow reversal where the strain is 0 and the shear rate is maximum. From the star marker, the deformation proceeds through the circle point which corresponds with the onset of non-linear effects in the start-up prior to the stress overshoot. The square point is positioned beyond the stress overshoot and corresponds to the transition to primarily viscous flow. Qualitatively, comparing the transient moduli to the other parameters emphasizes the microstructural differences between the branched and unbranched micelles. The most dramatic differences arising due to the span of G_t' for the branched case, which covers a larger range of moduli values as compared to the unbranched case. Comparing the AF between unbranched and branched micelle solutions, we see that the overall degree of alignment acquired during this elastic dominated phase is far less for the branched micelles. While this is consistent with 6, SPP shows that the alignment achieved for the branched chains is almost constant during this phase of the cycle where the unbranched chains achieve their maximum alignment near the stress overshoot. We also see that during this elastic period, the AF remains tightly coupled to $\hat{\varepsilon}''$, mirroring the response under steady flow. However, from the stars to the squares in Figure 7 we see that this correlation is broken in the unbranched sample.

To compare this response as a function of Wi, we define the strain acquired since flow reversal for this half-cycle as γ_r. This representation emphasizes the startup phase of the LAOS half-cycle and allows us to focus on changed in dielectric properties that result from elastic effects. We used the corners identified in SPP (stars, squares, and circles) to correlate the elastic response of $\hat{\varepsilon}''$, G_t', and σ versus γ_r in Figure 7(b) for all points within the half-cycle. Note that the symbols from Figure 7 (a) are provided

for consistency. With increasing Wi, the strain and the stress at overshoot increases. Further, the apexes associated with the minimum in G_t'' (circle) is associated with larger strains at larger Wi for the branched and unbranched sample. A negative peak in G_t' and a local minimum in $\hat{\varepsilon}''$ also correspond to minimum in G_t' (squares). This observation is consistent with the breaking of chain ends at the point of maximum extension of the micelle network where a negative G_t' was shown previously to originate form the liberation of chain ends leading to elastic recovery.[49] While the alignment of the chains increases during this period of the startup, ε'' does not and instead decreases. This is counter to the case observed in steady flow where the high frequency dielectric response is determined by the alignment of the micelle segments. Nonetheless as the sample transitions to a primarily viscous response, the correlation observed under steady flow conditions is restored and ε'' increases with the Wi for strains beyond the minimum in G_t'' (circles). Beyond the stress overshoot, the network is able to partially recover its elasticity as indicated by the positive G_t'. $\hat{\varepsilon}''$ reaches its maximum for the branched micelles whereas the ε'' continues to increase the viscous response becomes dominant. At these larger values of strain the elasticity of the network is destroyed and the sample experiences primarily a viscous response as evidenced by the increase in G_t''.

At the same time, Figure 6 shows that the maximum AF occurs at point of maximum stress during the start-up phase of the LAOS cycle. This is in contrast to the branched sample where the maximum AF occurs during the viscous phase of the LAOS cycle where elastic effects are negligible. We speculate that the difference in AF arises because the branched sample is able to yield via a mechanism that is inaccessible to the unbranched sample, the breaking of branch points. Such a yielding mechanism would allow stress to relax without also leading to an increase in alignment that's associated with elastic processes. In contrast to the unbranched sample, the low frequency $\hat{\varepsilon}' < 0$ as shown in Figure 6 and 7b throughout the LAOS cycle. In Riley et al.[27], this behavior was attributed to the enhanced breakage rate of micelles under steady shear, the enhanced real component of the permittivity at low frequencies attributed to the breakage of system spanning branch connections. This phenomena manifests as a negative value of $\hat{\varepsilon}'$ at low frequencies. While the breaking of branched segments is a primarily viscous process, these branched segments can rapidly recover during flow reversal as the shear rate is zero. During this period we see evidence of network recoil, followed by rapid network recovery. This effect is most pronounced in the $Wi = 10$ case, where the trajectory from stars to squares to circles occurs over only a few strain units after reversal. These observations would be very difficult to identify without the combination of time-resolved, frequency dependence dielectric measurements during transient LAOS and the use of SPP to divide the LAOS cycle into predominantly viscous and elastic responses.

7 Conclusions

We have examined the microscopic dynamics of branched and unbranched inverse WLMs subjected to the steady and transient LAOS flow using rheo-dielectric and rheo-SANS techniques. The dielectric rheology protocol explored here utilizes time-dependent oscillatory shear to probe the transient frequency-dependent complex permittivity of the unbranched and branched WLMs in LAOS flow as the function of Wi. The observed transient stress response for both unbranched and branched WLM solutions could not be used to uniquely identify the presence of branch points. However, when this transient stress was combined with frequency dependent dielectric signals, it was possible to distinguish how the topological differences between the samples influences the transition to non-linear flow. This work further compared the rich features of the dielectric response of both samples to the development of anisotropy at segmental length scales using rheo-SANS. From the change in anisotropy throughout the cycle, the evolution of the microstructure was correlated with the evolution of the dielectric response. We observed that the degree of the maximum alignment was improved as increasing Wi for both samples. However, a crucial difference was observed during LAOS where a maximum in anisotropy factor occurred near the position of the maximum stress in the cycle in the unbranched sample but not in the branched sample. This indicates that the stress overshoot in the branched sample is correlated with a primarily viscous response.

These findings reveal the value of frequency dependent dielectric measurements during transient flow and support using SPP analysis to isolate elastic effects in the transient flow. This analysis showed that upon flow reversal the elastic response originates from reorientation of the Kuhn segments dominating the material response as the shear rate increases. The unbranched sample behaves similarly to the branched sample throughout the deformation except for the large transient modulus in the branched WLMs. These observations of transient modulus are consistent with acquiring broken segments with the stretched entangled network, which leads to enhanced viscous dissipation and elastic recoil. However, compared with the signature of the strong alignment with transient modulus for the unbranched sample, the branched sample shows no significant increases in the anisotropy factor. In so doing, we extend the insight gained by performing LAOS tests on these complex materials.

Author Contributions

N.C., J.K.R and J.R. conceptualized the work. N.C., R.M., and J.J.R. performed the experiments, analyzed the data, and wrote the original draft. J.S. and S.R. performed the SPP calculation and contributed to the writing and revision of the manuscript. All authors discussed the results and have given approval to the final version of the manuscript.

Conflicts of interest

J.J.R. reports financial support from the National Science Foundation and the Department of Energy.

Acknowledgements

The authors acknowledge support for the VSANS beamline from the Center for High Resolution Neutron Scattering (CHRNS), a national user facility jointly funded by the NCNR and the NSF under Agreement No. DMR-2010792. We appreciate numerous discussions with Steve Kline regarding the strategy of anal-

ysis of time-resolved SANS data. N.H.C. would like to recognize ACS PRF Award 60442-DNI6 for support during the completion of experimental works. JS and SAR acknowledge support from the National Science Foundation under the DMREF Awards DMR-2119172. The authors thank Steve Kline and Brian Maranville for fruitful discussions regarding event mode data processing. Commercial equipment and materials identified in this work is not intended to imply recommendation or endorsement by NIST.

Notes and references

1 R. Angelico, U. Olsson, K. Mortensen, L. Ambrosone, G. Palazzo and A. Ceglie, *Journal of Physical Chemistry B*, 2002, **106**, 2426–2428.

2 J. F. Berret, D. C. Roux and P. Lindner, *European Physical Journal B*, 1998, **5**, 67–77.

3 M. A. Calabrese, S. A. Rogers, R. P. Murphy and N. J. Wagner, *Journal of Rheology*, 2015, **59**, 1299–1328.

4 R. Mhanna, J. Lee, S. Narayanan, D. H. Reich and R. L. Leheny, *Nanoscale*, 2019, **11**, 7875–7884.

5 P. Schurtenberger, L. J. Magid, J. Penfold and R. Heenan, *Langmuir*, 1990, **6**, 1800–1803.

6 P. E. Boukany and S. Q. Wang, *Macromolecules*, 2008, **41**, 1455–1464.

7 C. J. Dimitriou, L. Casanellas, T. J. Ober and G. H. McKinley, *Rheologica Acta*, 2012, **51**, 395–411.

8 M. W. Liberatore, F. Nettesheim, P. A. Vasquez, M. E. Helgeson, N. J. Wagner, E. W. Kaler, L. P. Cook, L. Porcar and Y. T. Hu, *Journal of Rheology*, 2009, **53**, 441–458.

9 H. Mohammadigoushki and S. J. Muller, *Soft Matter*, 2016, **12**, 1051–1061.

10 S. Kim, J. Mewis, C. Clasen and J. Vermant, *Rheologica Acta*, 2013, **52**, 727–740.

11 R. Angelico, L. Gentile, G. A. Ranieri and C. O. Rossi, *RSC Advances*, 2016, **6**, 33339–33347.

12 C. Lepper, P. J. Edwards, R. Dykstra and M. A. Williams, *Soft Matter*, 2011, **7**, 10291–10298.

13 T. Kida, Y. Hiejima and K. hei Nitta, *Macromolecules*, 2019, **52**, 4590–4600.

14 A. P. Kotula, M. W. Meyer, F. D. Vito, J. Plog, A. R. H. Walker and K. B. Migler, *Review of Scientific Instruments*, 2016, **87**, 105105.

15 R. L. Leheny, M. C. Rogers, K. Chen, S. Narayanan and J. L. Harden, *Current Opinion in Colloid and Interface Science*, 2015, **20**, 261–271.

16 M. C. Rogers, K. Chen, M. J. Pagenkopp, T. G. Mason, S. Narayanan, J. L. Harden and R. L. Leheny, *Physical Review Materials*, 2018, **2**, 1–11.

17 X. D. Pan and G. H. McKinley, *Journal of Colloid and Interface Science*, 1997, **195**, 101–113.

18 H. Watanabe, *Macromolecular Rapid Communications*, 2001, **22**, 127–175.

19 W. H. Stockmayer, *Pure and Applied Chemistry*, 1967, **15**, 539–554.

20 J. J. Richards and J. K. Riley, *Current Opinion in Colloid and Interface Science*, 2019, **42**, 110–120.

21 S. Höfl, F. Kremer, H. W. Spiess, M. Wilhelm and S. Kahle, *Polymer*, 2006, **47**, 7282–7288.

22 R. H. Colby, D. C. Boris, W. E. Krause and J. S. Tan, *Journal of Polymer Science, Part B: Polymer Physics*, 1997, **35**, 2951–2960.

23 F. Bordi, R. H. Colby, C. Cametti, L. de Lorenzo and T. Gili, *Journal of Physical Chemistry B*, 2002, **106**, 6887–6893.

24 F. Bordi, C. Cametti and R. H. Colby, *Journal of Physics Condensed Matter*, 2004, **16**, R1423–R1463.

25 G. M. Newbloom, K. M. Weigandt and D. C. Pozzo, *Macromolecules*, 2012, **45**, 3452–3462.

26 D. Steinhauser, M. Möwes and M. Klüppel, *Journal of Physics Condensed Matter*, 2016, **28**, 495103.

27 J. K. Riley, J. J. Richards, N. J. Wagner and P. D. Butler, *Soft Matter*, 2018, **14**, 5344–5355.

28 J. J. Richards, J. B. Hipp, J. K. Riley, N. J. Wagner and P. D. Butler, *Langmuir*, 2017, **33**, 12260–12266.

29 H. Lin, M. V. Majji, N. Cho, J. R. Zeeman, J. W. Swan and J. J. Richards, *Proceedings of the National Academy of Sciences*, 2022, **119**, e2203470119.

30 A. Helal, T. Divoux and G. H. McKinley, *Physical Review Applied*, 2016, **6**, 064004.

31 K. Hyun, S. Höfl, S. Kahle and M. Wilhelm, *Journal of Non-Newtonian Fluid Mechanics*, 2009, **160**, 93–103.

32 K. Horio, T. Uneyama, Y. Matsumiya, Y. Masubuchi and H. Watanabe, *Macromolecules*, 2014, **47**, 246–255.

33 H. Watanabe, S. Ishida and Y. Matsumiya, *Macromolecules*, 2002, **35**, 8802–8818.

34 P. A. Cirkel and G. J. Koper, *Langmuir*, 1998, **14**, 7095–7103.

35 N. H. Cho, J. K. Riley and J. J. Richards, *The Journal of Physical Chemistry B*, 2021, **125**, 11067–11077.

36 P. A. Cirkel, M. Fontana and G. J. Koper, *Journal of Dispersion Science and Technology*, 2001, **22**, 211–219.

37 S. A. Rogers, B. M. Erwin, D. Vlassopoulos and M. Cloitre, *Journal of Rheology*, 2011, **55**, 435–458.

38 J. J. Richards, N. J. Wagner and P. D. Butler, *Review of Scientific Instruments*, 2017, **88**, 105115.

39 J. Barker, J. Moyer, S. Kline, G. Jensen, J. Cook, C. Gagnon, E. Kelley, J. P. Chabot, N. Maliszewskyj, C. Parikh, W. Chen, R. P. Murphy and C. Glinka, *Journal of Applied Crystallography*, 2022, **55**, 271–283.

40 S. R. Kline, *Journal of Applied Crystallography*, 2006, **39**, 895–900.

41 S. A. Rogers, *Rheologica Acta*, 2017, **56**, 501–525.

42 G. J. Donley, J. R. de Bruyn, G. H. McKinley and S. A. Rogers, *Journal of Non-Newtonian Fluid Mechanics*, 2019, **264**, 117–134.

43 J. C.-W. Lee, L. Porcar and S. A. Rogers, *Polymers*, 2019, **11**, 1189.

44 J. D. Park and S. A. Rogers, *Journal of Rheology*, 2018, **62**, 869–888.

45 L. M. Walker and N. J. Wagner, *Macromolecules*, 1996, **29**, 2298–2301.

46 M. M. Britton and P. T. Callaghan, *Physical review letters*, 1997, **78**, 4930.

47 E. Cappelaere, J. F. Berret, J. P. Decruppe, R. Cressely and P. Lindner, *Physical Review E*, 1997, **56**, 1869.

48 J. Choi, F. Nettesheim and S. A. Rogers, *Physics of Fluids*, 2019, **31**, 073107.

49 S. Rogers, J. Kohlbrecher and M. P. Lettinga, *Soft Matter*, 2012, **8**, 7831–7839.